

PHD RESEARCH PROPOSAL FOR ICRAR / UWA

SIX-MONTH REVIEW

**Environmental effects on Spatially-resolved Star Formation and
Interstellar Medium Properties in the Virgo Cluster**

Student:

Rongjun Huang^{ID}

Rongjun.Huang@icrar.org

UWA ID: 22402136

Supervisors:

Prof. Luca Cortese

A/Prof. Luke Davies

Panel:

Prof. Kenji Bekki

A/Prof. Claudia Lagos Urbina



International
Centre for
Radio
Astronomy
Research



Submitted in partial fulfilment of the requirements for the degree of Doctor of Philosophy in

Astrophysics

at The University of Western Australia

August 25, 2025

Abstract

Galaxy evolution is predominantly governed by the balance between gas supply, star formation, and metal enrichment; while over-dense environments can perturb this balance, impacting the galaxy evolution process. Leveraging the state-of-the-art MAUVE-MUSE and MAUVE-ALMA observations of 40 Virgo late-type galaxies at ~ 100 pc resolution, this project will test whether a spatially-resolved fundamental metallicity relation (rFMR) exists and how it varies with environment. First, we will map the rFMR surface across all available galaxies' inner discs to study its existence and quantify cluster-driven offsets. Second, we will incorporate molecular and atomic gas to evaluate whether gas content explains the scatter in the resolved Star Forming Main Sequence and yields a tighter rFMR plane when substituted for gas-phase metallicity. Additionally, we will explore a stellar rFMR by replacing gas-phase with stellar metallicity to connect present enrichment to past star-formation histories. Together, these steps deliver an environmentally aware, spatially-resolved view of how gas, stars, and metals co-regulate galaxy evolution in a dense cluster environment.

1 Research Project

1.1 Literature Review

1.1.1 The “Bathtub” Self-Regulation Model

An effective and powerful framework for galaxy formation and evolution is the self-regulation model (a.k.a., “reservoir”, “open-box” or “bathtub” model), which envisions a galaxy’s gas reservoir like water in a tub controlled by inflow and outflow (e.g., [Bouché et al., 2010](#); [Davé et al., 2012](#); [Krumholz & Dekel, 2012](#); [Lilly et al., 2013](#); [Bouché, 2017](#); [Rybizki et al., 2017](#); [Wang & Lilly, 2023](#)). This simple regulator concept was first described in analytic form and named as “reservoir” by [Bouché et al. \(2010\)](#) or “bathtub” by [Davé et al. \(2012\)](#); [Krumholz & Dekel \(2012\)](#). [Lilly et al. \(2013\)](#) later generalized it by allowing the gas reservoir to evolve, formulating a gas-regulator model where the instantaneous gas mass adjusts to track the gas flow. In this “bathtub” model, the inflow of fresh gas from the intergalactic medium (IGM) fuels star formation, while star formation itself consumes gas via the collapse of Giant Molecular Clouds (GMCs) and drives outflows via galactic feedback. The system rapidly adjusts toward an equilibrium where the star formation rate (SFR) balances the net gas accretion rate, keeping the gas mass roughly constant over time. In other words, galaxies self-regulate: if gas inflow increases, star formation (and outflows) will rise until a new balance is reached, and vice versa (see [Figure 1.1](#) for the visualization of this “bathtub” model).

The galactic scaling relations that emerge from this “bathtub” framework are well-established to describe the interconnected nature of the gas cycle, star formation, and metal abundances in galaxies, forming a coherent picture of galaxy evolution. Here we briefly review these key relations and interpretations of them, especially including results from spatially-resolved observations in the local universe, which provide a more nuanced view inside galaxies. Such spatially-resolved observations have only become feasible with the development of large-scale Integral Field Unit (IFU) spectroscopic surveys in the past decade, e.g., SAMI (Sydney-Australian Astronomical Observatory Multi-object Integral field spectrograph; [Croom et al., 2012](#)), CALIFA (the Calar Alto Legacy Integral Field Area; [Sánchez et al., 2012](#)), MaNGA (Mapping Nearby Galaxies at APO; [Bundy et al., 2015](#)), GASP (Gas Stripping Phenomena in Galaxies with MUSE; [Poggianti et al., 2017](#)), MAGPI (Middle Ages Galaxy Properties with Integral Field Spectroscopy; [Foster et al., 2021](#)), and PHANGS (Physics at High Angular resolution in Nearby Galaxies; [Emsellem et al., 2022](#)).

One of the natural outcomes of the self-regulation model is to provide a framework for the gas–star formation cycle in galaxies. [Lilly et al. \(2013\)](#) showed that, assuming a roughly constant star-formation efficiency and wind mass-loading (fraction of gas expelled), the galaxy’s specific SFR ($\text{sSFR} = \text{SFR}/M_*$)

naturally equals the specific accretion rate of its dark halo in equilibrium. This explains the observed correlation between M_* and SFR known as the star-forming main sequence (SFMS). Empirically, at $z \sim 0$ the SFMS is roughly linear (slope $\sim 0.7-1$) with ~ 0.3 dex scatter and shows a high-mass flattening likely linked to quenching (e.g., [Speagle et al., 2014](#); [Whitaker et al., 2014](#); [Leslie et al., 2020](#); [Thorne et al., 2021](#)). In the spatially resolved sense, the same trend holds within disks: regions of higher stellar-mass surface density (Σ_*) form stars at higher surface densities (Σ_{SFR}), i.e. the resolved SFMS (rSFMS) on kpc and even sub-kpc scales (e.g., [Cano-Díaz et al., 2016](#); [Hsieh et al., 2017](#); [Pessa et al., 2021](#); [Baker et al., 2023](#)). Early IFU work (CALIFA, SAMI, MaNGA, PHANGS) established and quantified this local law, and recent analyses indicate that it emerges naturally from two more fundamental relations—the resolved molecular-gas main sequence (rMGMS) and the resolved Kennicutt–Schmidt law (rKS) ([Baker et al., 2022](#)). Consistent with the regulator picture, the gas consumption/depletion time ($\tau_{\text{dep}} = M_{\text{gas}}/\text{SFR}$) is observed to be much shorter than the age of the Universe (e.g., $\tau_{\text{dep}} \sim 1.5$ Gyr at $z \sim 0$ and $\tau_{\text{dep}} \sim 0.5$ Gyr at $z \sim 1-2.5$; [Genzel et al., 2010](#)), implying that continuous inflow is required to sustain SFRs over cosmic time ([Bouché, 2017](#)). In dense environments such as the Virgo Cluster, processes that modulate inflow/outflow will shift the equilibrium, but do not negate self-regulation.

Moreover, the regulator model also predicts how galaxies enrich with metals. In the “bathtub” framework, the gas-phase metallicity rapidly converges to an equilibrium set by the competition between metal production, dilution by pristine inflow, and removal/retention in outflows ([Lilly et al., 2013](#)). This balance naturally reproduces the integrated mass–metallicity relation (MZR), which is a steep low-mass rise with high-mass saturation, small scatter, and a redshift evolution toward lower metallicities at earlier times (e.g., [Tremonti et al., 2004](#); [Curti et al., 2020](#); [Sanders et al., 2021](#)). On resolved scales, a tight rMZR is observed: local Z_{gas} increases smoothly with Σ_* across disks, recovering both global MZR trends and radial metallicity gradients (e.g., [Sánchez et al., 2013](#); [Barrera-Ballesteros et al., 2016](#)). Extensions to spatially resolved discs show that individual annuli settle into local chemical equilibrium, together recreating observed gradients without fine-tuned merger histories ([Belfiore et al., 2019](#)).

Overall, the self-regulation “bathtub” model offers a galaxy evolution framework: galaxies gradually convert inflowing gas into stars, while outflows prevent runaway growth, yielding stable SFRs and predictable chemical enrichment mechanisms. It ties together the star formation history (SFH), and the scaling relations of gas and metals in galaxies, including global view and spatially-resolved scale. The success of this model suggests that even complex galaxy processes (e.g., cooling, feedback, merging, interaction, etc.) tend to drive systems toward an equilibrium that can be simply described by a few global and/or local parameters. This provides a useful guiding framework for interpreting observations of nearby late-type galaxies (like those in the Virgo Cluster) as a self-regulating mechanism where gas inflow/outflow, star formation, and metal enrichment are in balance.

1.1.2 From “Bathtub” model to FMR

With SFMS and MZR in hand, it becomes obvious to ask whether these relations might be interconnected – after all, stellar mass, star formation rate, and metallicity are all fundamental properties that should be physically linked through a galaxy’s evolutionary history. This intuitive reasoning leads astronomers to explore the fundamental metallicity relation (FMR), which refers to the empirical discovery that a galaxy’s metallicity is tightly correlated with both its stellar mass and SFR, forming a 3D surface in $Z(M_*, \text{SFR})$

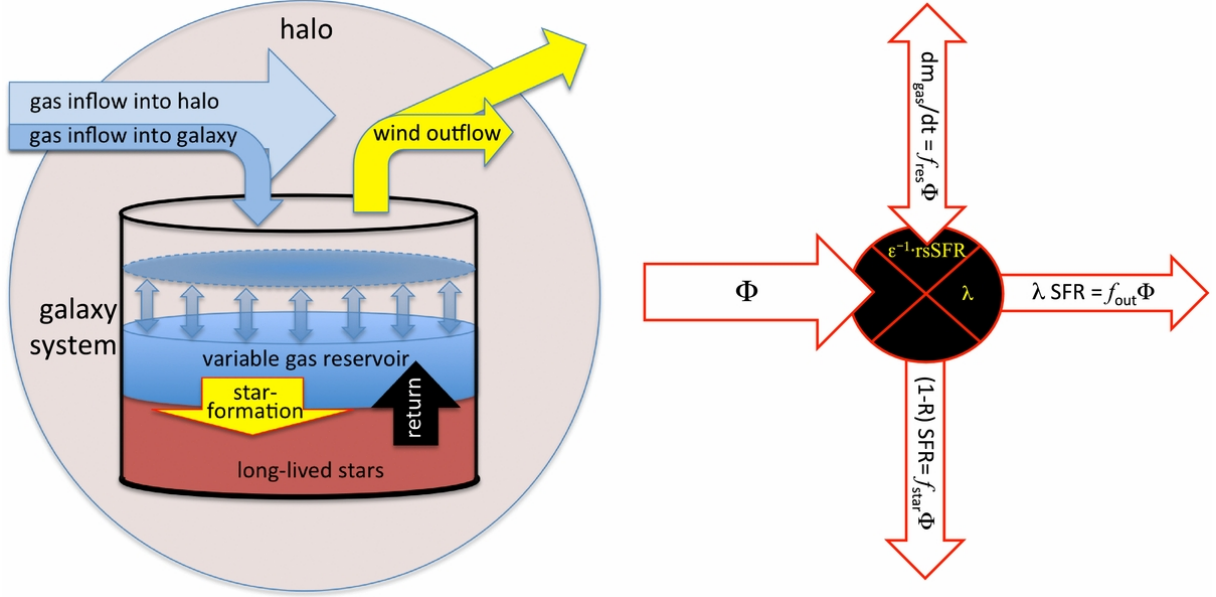


Figure 1.1: The “bathtub” (gas-regulator) model of Lilly et al. (2013). Left: gas accretes into the halo; a fraction f_{gal} reaches the galaxy at rate Φ and feeds a reservoir whose mass self-regulates the SFR. Stars form from this reservoir with efficiency ϵ (gas consumption time τ_{gas}), promptly returning some mass and newly produced metals to the ISM. Outflows Ψ , taken to scale with the SFR with mass-loading λ , eject gas from the system (and possibly the halo). The reservoir mass is free to vary and thus controls the SFR. Right: schematic of the net flows; the partition of the inflow Φ into star formation, outflow, and retention is set by ϵ , λ , and the sSFR, which vary slowly compared to the residence time τ_{gas} .

space. In 2010, two groups independently reported this three-parameter relationship (Mannucci et al., 2010; Lara-López et al., 2010). Mannucci et al. (2010) showed that SFGs define a surface in the 3D space of M_* –SFR– Z up to cosmic noon such that, 1) more massive galaxies are systematically more metal-rich, and 2) among galaxies of similar mass, those with higher star formation rates exhibit lower metallicities. In other words, the MZR is modulated by SFR: low-mass SFGs are offset to lower metallicity, whereas high-mass or more quiescent galaxies approach the metallicity ceiling (Bothwell et al., 2016). Around the same time, Lara-López et al. (2010) independently discovered such a “fundamental plane” relating stellar mass, metallicity, and SFR in the local universe. Both groups reported that this 3D relation has remarkably small scatter (on the order of 0.05 dex in metallicity) and thus captures an essential aspect of galaxy evolution (Mannucci et al., 2010; Lara-López et al., 2010). They claimed it “fundamental” because not only does this 3D relation appear to hold universally for SFGs and to remain roughly invariant with redshift out to at least $z \sim 2 - 3$, but the introduction of SFR as a second parameter also significantly reduces the scatter observed in the MZR.

This invariance suggests that the well-known redshift evolution of the integrated MZR can be largely explained by selection effects: high- z observations sample galaxies with higher SFRs (on average) which occupy a different part of the FMR, rather than an evolution of the relation itself. Subsequent observations have largely supported these findings. Numerous intermediate- and high- z surveys (e.g. at $z \sim 1-3$) have found that their galaxy samples are broadly consistent with the local FMR (e.g., Yates et al., 2012; Bothwell et al., 2013; Peng & Maiolino, 2014; Bothwell et al., 2016; Gao et al., 2018; Cresci et al., 2019; Koller et al., 2024; Pallottini et al., 2025). At the higher redshift epoch now accessible thanks to the James Webb Space Telescope (JWST), there are indications that even the FMR may start to shift (as extreme gas

accretion at early times drives metallicities much lower, see [Pallottini et al., 2025](#)), but this remains an active area of research and beyond the scope of this study.

Given the global FMR, a natural question is whether an analogous relation holds on kpc scales within galaxies. As discussed previously, resolved studies have found a tight local mass–metallicity relationship. In contrast, the negligible Σ_{SFR} effect of resolved FMR (rFMR) was noted. For example, using 3000 H II regions of 150 CALIFA galaxies, [Sánchez et al. \(2013\)](#) found that local metallicity is almost entirely driven by Σ_* with no significant secondary dependence on SFR. An updated CALIFA analysis of 734 galaxies by [Sánchez et al. \(2017\)](#) confirmed that any hint of SFR dependence appeared only at the extreme low-mass end ($M_* < 10^{9.5} M_\odot$), where the data were incompleteness, and thus unclear. Similarly, MaNGA ([Barrera-Ballesteros et al., 2016](#)), SAMI ([Sánchez et al., 2019](#)) and MUSE-Wide ([Yao et al., 2022](#)) data challenge the existence of an rFMR in typical local star-forming galaxies –the data show a tight rMZR but essentially no residual metallicity dependence on local star formation activity across most of the parameter space.

However, [Cresci et al. \(2019\)](#) revisited the CALIFA and MaNGA samples and found that the same datasets were actually consistent with the traditional FMR when analyzed using the original [Mannucci et al. \(2010\)](#) formulation. By fitting a 3D surface to M_* , SFR, and Z , they recover the expected anti-correlation: at fixed stellar mass, regions (or galaxies) with higher SFR have slightly lower metallicity, in agreement with FMR predictions. The discrepancy with earlier findings appears to lie in methodology, such as whether one examines residuals of a polynomial fit versus directly fitting a 3D plane, how one handles biases in sample selection, and which metallicity calibration is adopted. In addition, a recent study by [Baker et al. \(2023\)](#) found that resolved metallicity is influenced by both local and global factors. Using MaNGA galaxies, they reported that while Σ_* and Σ_{SFR} set a baseline local relation, a galaxy’s total stellar mass also imposes a modest offset (i.e. regions in a more massive galaxy are on average more metal-rich at fixed local Σ_*), implying a combined local+global FMR. These results suggest that a weak resolved FMR may exist, even if the dominant driver is still the local stellar mass density (see [Figure 1.2](#) for visualization of rFMR). With the high sensitivity of VLT/MUSE, the existence of rFMR is further validated with recent studies by [Bulichi et al. \(2023\)](#) and [Koller et al. \(2024\)](#).

The existence and form of the FMR can be explained by the balance of galactic inflows, outflows, and star formation activities. The anti-correlation between SFR and metallicity at fixed mass is a natural outcome that a high SFR indicates the galaxy is experiencing a high gas accretion rate (fueling a starburst). The accreted pristine gas is metal-poor, so it dilutes the ISM metallicity even as it boosts star formation ([Mannucci et al., 2010](#)). Conversely, a galaxy with a low sSFR (low SFR relative to its mass) likely hasn’t accreted much new gas recently, allowing its existing gas to remain enriched or even become metal-rich as stars continue to synthesize elements. In effect, infall drives the SFR– Z anticorrelation by simultaneously lowering Z and raising SFR. On the other hand, the stellar mass dependence of metallicity is attributed to cumulative metal retention: massive galaxies have deeper potentials and can retain metals (and/or funnel fresh gas into central star formation) more effectively, whereas low-mass galaxies lose a larger fraction of metals to winds. This introduces the primary M_* – Z slope, on top of which the SFR modulates the metallicity. [Mannucci et al. \(2010\)](#) proposed that infall is the dominant effect at high redshift (or lower-mass, high-SFR galaxies), while outflow feedback dominates at low redshift (or higher-mass, low-SFR galaxies), and together with the star formation law, these processes shape the FMR. The significantly small scatter about the FMR (only ~ 0.05 dex) supports the idea of a fairly tight equilibrium: most SFGs

up to $z \sim 3$, lie on a smoothly varying sequence, rather than undergoing wildly stochastic enrichment events. Furthermore, spatially-resolved investigations of the FMR reveal that local metallicity cannot be explained by local processes alone, but instead depends on both local and global galactic properties. [Baker et al. \(2023\)](#) found that resolved metallicity shows a strong dependence on total stellar mass and a weaker inverse dependence on total SFR, suggesting that global processes (e.g., the global gravitational potential well, galactic winds, and global metal mixing or redistribution) significantly influence local metallicity patterns. Such phenomenon is more prominent in dwarf galaxies ([Bulichi et al., 2023](#)). Similar results were confirmed in a recent study on MAGPI galaxies by [Koller et al. \(2024\)](#) and they also observed that rFMR is tighter at lower stellar mass. This finding that rFMR depends on total stellar mass implies that the rFMR may be sensitive to environmental effects that modulate these global processes, potentially causing the deviation of rFMR in cluster environments (e.g., the Virgo Cluster).

The FMR’s consistency with theory is further evidenced by simulations and models. Numerical cosmological simulations (as well as analytic and semi-analytic models) have been able to reproduce the FMR in its general form ([Bothwell et al., 2016](#)). For example, equilibrium models by [Davé et al. \(2012\)](#) and [Dayal et al. \(2013\)](#) naturally yield a constant FMR over cosmic time; while semi-analytic approaches (SAM; e.g., [Yates & Kauffmann, 2014](#)), smoothed particle hydrodynamics (SPH; e.g., [Obreja et al., 2014](#)) and cosmological hydrodynamics (e.g., [Garcia et al., 2024](#)) simulations likewise produce the FMR similar to observations. These models typically invoke the “bathtub” scenario, where inflow, star formation, and outflow reach a steady state. For example, the metallicity can be expressed as

$$Z \propto \frac{y}{\dot{M}_{\text{in}}} \left(1 - \text{SFR}^{-\frac{\dot{M}_{\text{in}}}{\dot{M}_{\text{in}} - \dot{M}_{\text{out}}}} \right), \quad (1.1)$$

with \dot{M}_{in} and \dot{M}_{out} denoting the gas inflow and outflow rate, respectively ([Dayal et al., 2013](#)); while the stellar mass is simply the integration of SFR over time. Overall, the FMR is viewed as strong evidence for self-regulation in galaxies: it demonstrates how galaxies of a given mass tend toward an equilibrium where inflowing gas feeds star formation and dilutes metals, while feedback and past star formation set the baseline metallicity. Any theoretical approach of galaxy evolution must explain not just the existence of the MZR and the SFMS, but also the fact that these two are linked in an inherent non-evolving 3D relation, the FMR.

Moreover, there exist some varieties or extensions of the FMR. One variety is that the SFR dependence in the FMR is likely a consequence of a more fundamental dependence on gas content: galaxies with larger gas reservoirs both form stars more rapidly and have more dilution of metals, so gas mass can be a natural third parameter. [Bothwell et al. \(2013\)](#) found a tight relation between M_* , metallicity, and H I gas mass (the “H I-FMR”). Later, [Bothwell et al. \(2016\)](#) showed that molecular or total gas mass is a key driver: at fixed stellar mass, metallicity anti-correlates more strongly with a galaxy’s molecular or total gas mass than with its SFR. In other words, the underlying “fundamental” relation may be between mass, metallicity, and gas content, with SFR entering only indirectly via the KS law (since more gas fuels higher SFR). However, a recent study by [Baker et al. \(2023\)](#) contradicted this finding and they argued that such relation is still unclear because the traditional CO-H₂ conversion (α_{CO}) is metallicity-dependent. Another extension is the so-called “stellar FMR”. While the classic FMR deals with gas-phase metallicity, recent work has asked whether a similar 3D relation exists for the average metallicity of stellar populations. [Looser et al. \(2024\)](#) found a smooth correlation between M_* , SFR, and the light-weighted

Z_* of local galaxies. In this stellar-FMR, starburst galaxies tend to have younger, more metal-poor stellar populations, whereas more passive galaxies have older, metal-rich stars. This implies that the integrated SFH of a galaxy also reflects the FMR pattern: systems that sustained high SFRs (often due to ample gas inflow) not only have lower gas-phase metallicities, but over time they build up stellar populations that are slightly lower in metallicity as well, and hence suggest a continuity between the instantaneous gas-phase FMR and the long-term chemical evolution imprinted in stars (Looser et al., 2024).

1.1.3 Environment effects on scaling relations in cluster galaxies

While the scaling relations reviewed in subsection 1.1.2 are well-established in studies of field galaxies, their behavior in cluster environments remains poorly characterized. Investigating how environmental processes modify these fundamental relations is crucial for constraining theoretical models of galaxy evolution and quenching mechanisms in dense environments. In nearby clusters, the SFMS has a similar slope to the field relation, but with significantly greater scatter due to environmental quenching (see also satellite SFR suppression at fixed mass in groups/clusters: Davies et al., 2019, 2025). For example, Boselli et al. (2023) used VESTIGE (A Virgo Environmental Survey Tracing Ionised Gas Emission) data for 384 Virgo Cluster galaxies and found the SFMS slope in Virgo is comparable to that in the field, yet the dispersion is $\sim 3\times$ larger (≈ 1 dex). This increased scatter is driven by H I-stripped cluster galaxies that lie far below the normal SFMS, whereas Virgo galaxies with normal gas content still follow the usual sequence (Boselli et al., 2023). The sSFRs of gas-poor cluster spirals are much lower than H I-rich counterparts of the same mass, indicating ongoing quenching. Such observations strongly suggest outside-in quenching by ram-pressure stripping (RPS): rapid gas removal (quenching in < 1 Gyr) can produce the pronounced SFR deficit and wide SFMS scatter observed in clusters, ruling out milder processes like starvation alone (Boselli et al., 2023).

As for metal enrichment, several studies have found that star-forming cluster galaxies tend to be slightly more metal-rich than field galaxies of the same mass, but the difference is small ($\lesssim 0.05$ dex; e.g., Peng & Maiolino, 2014; Lian et al., 2019; Schaefer et al., 2019; Pilyugin & Tautvaišienė, 2024). For instance, satellite galaxies in the local universe are observed to have slightly higher [O/H] at fixed mass than centrals, especially at lower masses, with differences on the order of 0.05 dex (Schaefer et al., 2019). Moreover, field galaxies in equally high-density regions exhibited similar metallicity enhancements, indicating the MZR offset is due to environment (overdensity) rather than solely cluster membership (Ellison et al., 2009).

This trend that modest metallicity increases in satellites aligns with the “strangulation” (or “starvation”, see Cortese et al., 2021, for review) scenario, a quenching mechanism that a galaxy has its external cold gas supply shut off (Peng et al., 2015). Such galaxy continues forming stars using existing gas, which elevates the gas-phase metallicity over time (no metal-poor accretion to dilute the ISM). For example, Maier et al. (2016) found that infalling cluster galaxies lie on the normal FMR, whereas galaxies that have been accreted in the cluster longer exhibit metallicities (0.3 – 0.5 dex) higher than predicted by that relation; in contrast, cluster galaxies identified as first-infallers (still acquiring gas) had metallicities consistent with the usual FMR expected for their ongoing SFRs. Thus, cluster environment effects strongly influence chemical evolution: satellite galaxies, especially low-mass ones, rapidly become over-enriched once they lack fresh gas (Maier et al., 2016). Thus, the cluster environment causes galaxies to overshoot the FMR

plane as gas stripping reduces their SFR while leaving metallicity elevated, with this effect strongest for low-mass satellites that are most vulnerable to stripping and have minimal dilution from residual inflows (Maier et al., 2016).

Conversely, a galaxy undergoing a sudden gas inflow or starburst in a cluster (e.g. due to a tidal interaction or group merger) might temporarily lie below the normal FMR (lower metallicity for its SFR). Such cases are observed in the form of those diluted, metal-poor cluster galaxies in AC114 and other merging substructures (Andrade et al., 2024). Such galaxies have elevated SFRs and lowered metallicities, making them FMR outliers in the opposite sense, though these tend to be transient (after the burst, they may enrich quickly).

Beyond global relations, spatially-resolved observations of cluster galaxies have revealed environmental effects on sub-galactic scales, though key scaling relations remain largely unexplored. The rSFMS has been systematically studied in nearby clusters, with Boselli et al. (2023) demonstrating that H I-stripped Virgo galaxies lie up to 1 dex below the field rSFMS while H I-normal satellites remain on the sequence, and VERTICO (THE VIRGO ENVIRONMENT TRACED IN CO SURVEY) observations confirming that molecular gas truncation pushes many cluster spirals below the field relation. Environmental effects on metallicity distributions have been investigated primarily through gradient measurements rather than rMZR, with studies finding systematically flatter gradients in cluster satellites compared to field controls (Lian et al., 2019; Franchetto et al., 2021; Lara-López et al., 2022; Zabel et al., 2024). Similarly, no rFMR has been attempted for cluster galaxies, despite field studies demonstrating the feasibility of three-parameter in spaxel-scale analysis (e.g., Cresci et al., 2019; Baker et al., 2023). This represents a significant observational gap, as environmental processes are expected to create complex, spatially dependent departures from field scaling relations that can only be captured through resolved studies.

1.2 This Work

1.2.1 Scientific motivation

Galaxy evolution is fundamentally driven by the interplay between internal processes and external environmental factors. While the self-regulation paradigm outlined in subsection 1.1.1 describes how isolated galaxies maintain equilibrium through gas inflows, star formation, and outflows, galaxy clusters provide the most extreme environments in which to test how external perturbations disrupt or enhance this delicate balance (Boselli & Gavazzi, 2006; Boselli et al., 2014). Rich clusters contain only $\sim 5\%$ of local galaxies, yet they concentrate hundreds of systems into small volumes, yielding galaxy densities orders of magnitude higher than the field (Boselli et al., 2018). In such dense environments, galaxies experience frequent interactions with both the hot intracluster medium (ICM) and neighboring systems.

Hydrodynamic interactions with the ICM can ram-pressure strip a galaxy’s gas reservoir as it moves through the cluster at velocities of hundreds to thousands of km/s (Jaffé et al., 2018). Simultaneously, gravitational encounters, including tidal interactions, mergers, and harassment, become ubiquitous between close neighbours. Some galaxies also undergo pre-processing in groups before entering the main cluster, experiencing milder versions of these transformative processes (Boselli et al., 2018). As satellite disks rush through this hostile environment, they undergo ram-pressure stripping, starvation, tidal

harassment and fast pre-processing that can significantly affect the gas cycle, star formation and metal enrichment (e.g. [Boselli & Gavazzi, 2006](#); [Boselli et al., 2014](#); [Jaffé et al., 2018](#)).

The importance of studying nearby clusters lies in the fact that only neighbouring systems allow us to resolve and disentangle these processes in detail. While high-redshift surveys reveal global evolutionary trends, detailed observations of local clusters are essential to understand the physical mechanisms driving these trends. However, whether the equilibrium-driven scaling relations reviewed in [section 1.1](#) survive such a violent environment on kpc or even ~ 100 pc scales is largely unknown. The Virgo Cluster offers the ideal laboratory to address this fundamental question. As one of our nearest clusters ($D \simeq 16.5$ Mpc; [Mei et al., 2007](#)), The Virgo Cluster is close enough to resolve individual H II regions with 8-meter class telescopes, yet massive enough ($M_{\text{vir}} \sim 6.3 \times 10^{14} M_{\odot}$; [Kashibadze et al., 2020](#)) to host all relevant environmental processes.

The Virgo Cluster provides several unique advantages as a testbed for environmental physics. It is the richest cluster within ~ 35 Mpc, containing thousands of member galaxies spanning all morphological types at roughly the same distance, enabling direct like-for-like comparisons under different environmental conditions ([Boselli et al., 2018](#)). As a dynamically young cluster still assembling, the Virgo Cluster consists of a main virialized component around M87 plus several infalling galaxies merging into the system. Many galaxies are therefore caught in intermediate stages of passage, and thus the Virgo Cluster contains ongoing case studies of environmental processing, which are invaluable for testing theoretical models of these processes under realistic conditions. Furthermore, Virgo’s spiral-rich population makes it ideal to study SFGs during active transformation, while its cluster properties (e.g., dynamical mass, ICM temperature, and density) represent the more common over-dense environments where most cluster galaxies reside, better than extreme nearby clusters like Coma, Leo, Norma and Fornax ([Boselli et al., 2018](#)). By focusing on the Virgo Cluster, we can understand how processes like RPS, starvation, and tidal interactions regulate or disrupt the galaxy’s “bathtub” cycle in nature’s most demanding laboratory.

1.2.2 MAUVE

In this study, we use data from MAUVE (Multiphase Astrophysics to Unveil the Virgo Environment), a comprehensive multiwavelength program investigating how the cluster environment affects the gas–star formation cycle in 40 late-type Virgo Cluster galaxies ([Watts et al., 2024](#)). The program originated as an European Southern Observatory (ESO) Large Programme with the Multi Unit Spectroscopic Explorer (MUSE) on the Very Large Telescope (VLT), building upon molecular gas observations from the previous VERTICO survey conducted with the Atacama Large Millimeter/submillimeter Array (ALMA). MAUVE has since expanded to include dedicated ALMA observations at higher spatial resolution (~ 50 pc) and recently awarded Hubble Space Telescope (HST) imaging observations, forming the MAUVE-ALMA and MAUVE-HST components, respectively. The original and ongoing VLT/MUSE observation, MAUVE-MUSE, provides stellar and ionised gas maps at $\sim 100 - 200$ pc resolution across the full extent of star-forming discs, targeting galaxies at distinct infall stages: early infallers, systems approaching pericentre, and those having passed their first pericentre passage. As the first survey to deliver sub-kpc spectroscopy of late-type cluster galaxies across various environmental phases, MAUVE offers a unique opportunity to quantify how the cluster environment regulates the gas-star formation cycle and trace the evolutionary sequence of environmental quenching.

1.2.3 Objectives

1. **First project: The rFMR in a cluster.** Map the $Z(\Sigma_*, \Sigma_{\text{SFR}})$ surface for all MAUVE-MUSE disks. First is to check if the rFMR still exists in ~ 100 pc resolution. If it exists, then we can compare it across different galaxies. We hypothesise an offset or variation of the surface, driven by environmental effects.
2. **Second project: Gas content as the hidden variable.** Adding MUSE-ALMA H_2 data (and maybe MeerKAT H I data) to test if molecular gas mass 1) can better describe the scatter seen in rSFMS; 2) tighten the rFMR plane when replacing the gas-phase metallicity with molecular gas mass.
3. **Third and probably other projects (future years).** It is worth to check stellar rFMR variation, that is replacing the gas-phase metallicity with stellar metallicity. Further projects are still undecided.

In summary, this PhD program will deliver the spatially-resolved assessment of how the Virgo cluster environment affects the star formation and ISM properties that support modern galaxy evolution theory. By exploiting the unique MAUVE data, we aim to explore the universal validity of the “bathtub” model when galaxies are plunged into the dense cluster environment of the local Universe.

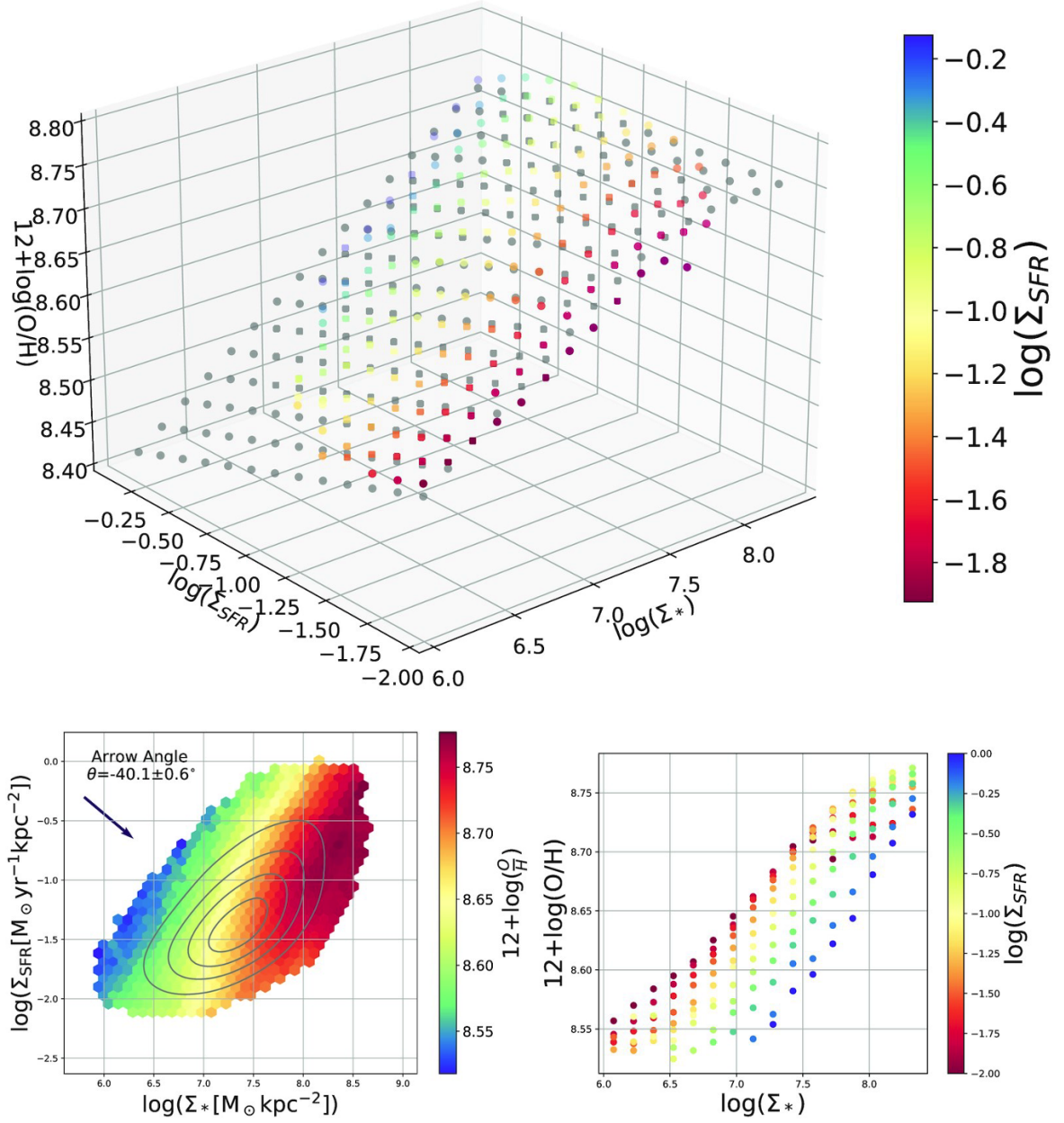


Figure 1.2: Top: surface of the resolved fundamental metallicity relation (rFMR) in $Z(\Sigma_*, \Sigma_{\text{SFR}})$ space from [Baker et al. \(2023\)](#). Bottom: projections of the rFMR in the Σ_* - Σ_{SFR} and Σ_* - Z planes, which correspond to the rSFMS and rMZR, respectively.

2 Data and Methodology

2.1 MAUVE–MUSE Datacubes and nGIST Value-added Products

The reduced MAUVE–MUSE datacubes employed in this work are taken from the **MAUVE** internal release v2 (IR v2) in December 2024, which currently contains 14 galaxies: IC 3392, NGC 4064, NGC 4192, NGC 4293, NGC 4298, NGC 4330, NGC 4383, NGC 4396, NGC 4419, NGC 4457, NGC 4501, NGC 4522, NGC 4694, and NGC 4698. Observations were obtained with MUSE in Wide Field Mode (WFM) on VLT/UT4, delivering a $60'' \times 60''$ field of view at $0.2'' \text{ pix}^{-1}$, a spectral sampling of $1.25 \text{ \AA pix}^{-1}$, and a nominal spectral resolution of $\text{FWHM} \simeq 2.5 \text{ \AA}$ at 7000 \AA . At the Virgo distance, the native spatial scale is $\sim 16 \text{ pc spaxel}^{-1}$ and typical seeing during the program delivers $\lesssim 100 \text{ pc}$ resolution. Reduction, sky subtraction, and flux calibration follow the workflow of [Emsellem et al. \(2022\)](#), executed with `pymusepipe` v2.28.2 and `esorex` 3.13.6, which wrap the MUSE data reduction scripts (DRS) version 2.8.7 ([Weilbacher et al., 2020](#)) and add exposure alignment and background–flux calibration steps. Each galaxy is delivered as a science-ready FITS cube whose *DATA*, *STAT*, and *DQ* extensions provide the flux, variance, and data–quality information across $4750\text{--}9350 \text{ \AA}$, respectively, on the native $0.2''$ grid (see also [Watts et al., 2024](#)).

All physical quantities analysed here are drawn from the nGIST value-added products ([Fraser-McKelvie et al., 2024](#)), a pPXF-based ([Cappellari, 2023](#)) wrapper (IR v2 products generated with nGIST v7.3) that provides a uniform set of stellar and ionised-gas maps for the MAUVE sample. The analysis adopts a Voronoi tessellation targeting $S/N = 40$ on the stellar continuum (measured over the optical range used by the survey); this single binning scheme is used as the common grid for all derived quantities, ensuring one-to-one correspondence between Σ_* , emission-line fluxes, and kinematics without additional resampling. Stellar continua and kinematics are modelled with pPXF using MILES SSP templates ([Vazdekis et al., 2015](#)), convolved to the wavelength-dependent MUSE line spread function (equation 8 in [Bacon et al. 2017](#)). Emission lines, strong sky lines, and the Na D absorption doublet are masked in the stellar fits; multiplicative Legendre polynomials absorb residual calibration mismatches and a [Calzetti](#)-like attenuation curve is included as a free parameter. After subtracting the best-fitting continuum, ionised-gas emission is measured by simultaneous Gaussian fitting of all prominent nebular lines (e.g. $\text{H}\alpha$, $\text{H}\beta$, $[\text{O III}]$, $[\text{N II}]$, $[\text{S II}]$). Following the survey convention, lines are grouped into Balmer, low-ionisation, and high-ionisation sets with velocities, dispersions and their corresponding fitting errors tied within each line; fixed line ratios are adopted for $[\text{O I}]$ 6364/6300 at 0.33, $[\text{N II}]$ 6548/6584 at 0.34, and $[\text{O III}]$ 4959/5007 at 0.35. The resulting maps include per-line fluxes, velocities, and velocity dispersions with formal uncertainties, together with the per-line instrumental broadening needed to recover intrinsic dispersions by quadrature subtraction. In this study, I use the following nGIST products: voronoi-binning maps

(*XXX_SPATIAL_BINNING_maps.fits*, where *XXX* is the ID of each galaxy), stellar kinematics maps (*XXX_KIN_maps.fits*), emission-line kinematics and intensity maps (*XXX_gas_BIN_maps.fits*), and light-weighted stellar populations and stellar extinction maps (*XXX_SFH_maps.fits*).

2.2 Stellar Mass Surface Density

I derive stellar mass surface densities on the nGIST Voronoi grid by combining per-bin stellar population weights with an *R*-band mass-to-light ratio matched to each bin's age-metallicity coordinates. For each bin of each galaxy, the SFH weights and the corresponding ($[M/H]$, $\log(\text{Age})$) grid is provided, and then I associate to every grid node an intrinsic $(M/L)_R$ drawn from a BaSTI-isochrone (Pietrinferni et al., 2013), Chabrier-IMF MILES library, and compute the light-weighted $(M/L)_R$ in each Voronoi bin by taking the SFH-weight dot-product with the tabulated $(M/L)_R$ values. This produces an *R*-band mass-to-light ratio map.

The observed *R*-band flux is measured directly from the MUSE cube using `spec-lite` (I use the `bessell-R` filter response to keep consistency with mass-to-light ratio map) to compute AB magnitudes per spaxel from the native flux-calibrated spectra (units of $10^{-20} \text{ erg s}^{-1} \text{ cm}^{-2} \text{ \AA}^{-1}$). I average fluxes within each Voronoi bin, convert back to magnitudes, and apply an internal attenuation correction using the nGIST $E(B-V)$ map and an $A_R/E(B-V)$ coefficient appropriate to the adopted filter response. I convert dereddened apparent magnitudes to absolute magnitudes and then to solar luminosities via $L_R/L_{R,\odot} = 10^{-0.4(M_R - M_{R,\odot})}$ (with $M_{R,\odot} = 4.65$ in AB magnitude). Stellar mass per Voronoi bin follows from

$$M_\star = L_R \cdot (M/L)_R, \quad (2.1)$$

and the stellar mass surface density is obtained by dividing by the physical bin area computed from the WCS pixel scales on the common grid¹:

$$\Sigma_\star = \frac{M_\star}{A_{\text{pix}}} [\text{M}_\odot \text{ kpc}^{-2}]. \quad (2.2)$$

2.3 Star Formation Rate Surface Density

2.3.1 Gas De-reddening

I measure emission-line fluxes on the same Voronoi grid used throughout this work and construct a Balmer decrement (BD) map from $H\alpha/H\beta$. A configurable quality-control scheme is applied to all lines; by default, I require $\text{Flux}/\text{Flux}_{\text{err}} \geq 3$ from pPXF fitting and a minimum flux floor of 20 (in the native unit of $10^{-20} \text{ erg s}^{-1} \text{ cm}^{-2}$) to define minimal detections. I also remove foreground stars using the `FOREGROUND_STAR` mask from the kinematic products when available.

The BD is defined as $\text{BD} = F_{H\alpha}/F_{H\beta}$, with two safeguards for physicality and upper-limit handling: (i) I floor low decrements to the Case B value, $\text{BD} \geq 2.86$; (ii) if a ratio is undefined but the underlying stellar

¹I have not yet accounted for disk inclination in surface density properties like Σ_\star here and Σ_{SFR} in next section; a future deprojection may be considered by multiplying these quantities by $\cos i$ for an adopted inclination i .

velocity is finite, I set $BD = 2.86$ and treat such spaxels as upper limits in subsequent SFR layers. I implement the [Calzetti](#) attenuation curve explicitly ($R_V = 4.05$), computing $k(\lambda)$ at each line wavelength, and convert BD to nebular color excess via

$$E(B-V)_{BD} = \frac{2.5}{k(H\beta) - k(H\alpha)} \log_{10} \left(\frac{BD}{2.86} \right), \quad (2.3)$$

then de-redden all relevant lines with

$$F_{\lambda, \text{corrected}} = F_{\lambda, \text{observed}} 10^{0.4 k(\lambda) E(B-V)_{BD}}. \quad (2.4)$$

For spaxels failing the Balmer detection criteria, I propagate an “upper-limit” treatment by replacing the corrected $H\alpha$ flux with $\max(\text{noise}, F_{H\alpha, \text{observed}})$ before converting to SFR, ensuring conservative SFR estimates in low-detection regions.

2.3.2 Ionization Classification and SF Masks

To isolate SF emission, I classify each spaxel on both the $[N\text{ II}]$ and $[S\text{ II}]$ BPT diagrams using the [Kauffmann et al. \(2003\)](#) and [Kewley et al. \(2001\)](#) curves for the $[N\text{ II}]$ plane and [Kewley et al. \(2001, 2006\)](#) for the $[S\text{ II}]$ plane. I build robust “classified” masks by propagating 1σ uncertainties on each logarithmic line ratio and requiring that the error-box remain within the same BPT region ($H\text{ II} + \text{composite}$ vs. AGN for $[N\text{ II}]$ BPT diagrams²; $H\text{ II}$ vs. LINER vs. Seyfert for $[S\text{ II}]$ BPT diagrams). Using these, I define four mutually exclusive categories per diagram: SF, non-SF, unclassified (detected but ambiguous at 1σ), and upper (insufficient Balmer information). I then combine the two diagrams with a default “both” logic: SF spaxels are those classified as SF in both $[N\text{ II}]$ and $[S\text{ II}]$ planes; non-SF are those classified (in both) but not SF; unclassified require $H\alpha$ and $H\beta$ detections but lack a robust class in at least one diagram; remaining spaxels are tagged as upper limits.

2.3.3 SFR Calibration

I convert dust-corrected $H\alpha$ luminosities to SFR using the [Calzetti et al. \(2007\)](#) relation adjusted to a [Chabrier](#) IMF,

$$\text{SFR}[M_{\odot} \text{ yr}^{-1}] = 4.98 \times 10^{-42} L_{H\alpha}^{\text{corr}} [\text{erg s}^{-1}], \quad (2.5)$$

with $L_{H\alpha}^{\text{corr}}$ is the corrected $H\alpha$ luminosity. I then form the SFR surface density by dividing by the pixel area derived from the WCS (kpc^2),

$$\Sigma_{\text{SFR}} = \frac{\text{SFR}}{A_{\text{pix}}} [M_{\odot} \text{ yr}^{-1} \text{ kpc}^{-2}]. \quad (2.6)$$

²In $[N\text{ II}]$ BPT diagrams, both $H\text{ II}$ and “Comp” regions are considered as ionization driven by star formation in this work.

2.4 Gas-phase Metallicity

I estimate gas-phase oxygen abundance, $12 + \log(\text{O}/\text{H})$, using two widely adopted strong-line calibrations applied to the de-reddened line maps from [section 2.3](#). First, I use the [D16](#) N2S2H α calibrator,

$$12 + \log(\text{O}/\text{H}) = 8.77 + y + 0.45 (y+0.3)^5, \quad (2.7)$$

where

$$y = \log\left(\frac{[\text{N II}]\lambda 6584}{[\text{S II}]\lambda\lambda 6717, 6731}\right) + 0.264 \log\left(\frac{[\text{N II}]\lambda 6584}{\text{H}\alpha}\right) \quad (2.8)$$

Second, I apply the [PG16](#) R3N2 S-calibration, which uses

$$N2 = \frac{[\text{N II}]\lambda\lambda 6548, 6584}{\text{H}\beta}, \quad S2 = \frac{[\text{S II}]\lambda\lambda 6717, 6731}{\text{H}\beta}, \quad R3 = \frac{[\text{O III}]\lambda\lambda 4959, 5007}{\text{H}\beta},$$

with a branch selection at $\log(N2) = -0.6$ and the published polynomial coefficients for the upper and lower branches (see equations 6 and 7 in [PG16](#)). As mentioned in [section 2.1](#), I rescale to doublet sums assuming $[\text{O III}]\lambda\lambda 4959, 5007 = 1.33 \times [\text{O III}]\lambda 5007$ and $[\text{N II}]\lambda\lambda(6548, 6584) = 1.34 \times [\text{N II}]\lambda 6584$ (as in [Watts et al. 2024](#)). For both methods, I adopt a validity range at 7.63–9.23 suggested by [Kewley et al. \(2019\)](#). To avoid bias from non-SF excitation, I apply metallicity calibrations only within the SF mask defined by my default “both” BPT logic, yielding two metallicity maps, $12 + \log(\text{O}/\text{H})_{\text{D16}}$ and $12 + \log(\text{O}/\text{H})_{\text{PG16}}$.

3 Project Plan

3.1 Project 1 —Resolved FMR in the Virgo Cluster at 100 pc (MAUVE–MUSE)

Goal: Establish the rFMR, $Z(\Sigma_*, \Sigma_{\text{SFR}})$, at ~ 100 pc for 14 Virgo late-type galaxies; quantify its intrinsic scatter, environmental offsets, and method systematics.

3.1.1 What's done so far (APR–AUG 2025; Mo 1–5)

- APR 2025: Data. Start with Legacy data and get familiar with MAUVE-MUSE datacube.
- APR-MAY 2025: Stellar continuum and M/L. Learn how to use pPXF; applying mass-to-light ratio; Σ_* maps produced on the same grid as binning maps; complete the pipeline to get Σ_* map.
- MAY-JUN 2025: Emission line and SFR. Check Quality Control; apply Balmer Decrement; distinguish the ionization mechanism by BPT diagrams; SFR calibration; complete the pipeline to get Σ_{SFR} map.
- JUL 2025: rSFMS. Construct rSFMS for individual galaxy and all SF spaxels; compare with previous works.
- AUG 2025: [O/H] map and rMZR. Acquire gas-phase metallicity map by using [D16](#) and [PG16](#) calibrations; construct rMZR for individual galaxy and all SF spaxels; compare with previous works; complete the pipeline to get [O/H] map.

3.1.2 Things to do (SEP 2025 - MAR 2026; Mo 6–12))

- SEP 2025: rSFMS and rMZR. Further analysis of these two scaling relations. Will check ionization parameter q .
- OCT-DEC 2025: rFMR. Construct rFMR for individual galaxy and all SF spaxels; further analysis and comparison with previous works: Partial Correlation Coefficient (PCC) analysis, 3D-surface fitting, intrinsic scatter, residual map, galaxy-by-galaxy analysis, environmental effects, etc.
- JAN-MAR 2026: Paper. Consolidate results, finalize figures/tables, archive products, submit Paper 1.

3.2 Project 2 —Gas as the hidden variable (MUSE–ALMA H₂; optional MeerKAT H I)

Goal: Test whether adding gas content tightens $Z(\Sigma_*, \Sigma_{\text{SFR}})$ by linking rSFMS scatter to Σ_{gas} and gas fractions; quantify environmental effects.

3.2.1 Things to do (APR 2026–MAR 2027; Mo 13–24)

- APR–JUN 2026: Data assembly and calibration. Collect ALMA CO products; derive Σ_{H_2} (choose/justify X_{CO}); ingest optional MeerKAT H I to get Σ_{HI} ; beam-match and align to MUSE grid; propagate uncertainties.
- JUL–SEP 2026: First analyses. rSFMS scatter vs gas fraction at fixed Σ_* ; partial correlations; re-fit rFMR with an explicit gas term (e.g. $Z(\Sigma_*, \Sigma_{\text{gas}})$).
- OCT–DEC 2026: Robustness and environment. Resolution and DIG tests; sensitivity to X_{CO} choices; offsets vs cluster phase-space; prepare figure/table templates.
- JAN–MAR 2027: Paper. Consolidate results, finalize figures/tables, archive products, submit Paper 2.

3.3 Project 3 —Stellar rFMR and enrichment history (Z_*)

Goal: Replace gas-phase Z_{gas} with stellar Z_* to probe enrichment history and timescales; relate stellar and gas-phase planes and their environmental dependence.

3.3.1 Things to do (APR 2027–MAR 2028; Mo 25–36)

- APR–JUL 2027: Stellar population maps. Full-spectrum fits (e.g. pPXF) to obtain Z_* , mass- and light-weighted ages; align with gas maps.
- AUG–OCT 2027: Construct stellar rFMR. Fit $Z_*(\Sigma_*, \Sigma_{\text{SFR}})$ per galaxy and stacked; compare shapes and intrinsic scatter to gas-phase rFMR; radial and arm/interarm controls.
- NOV 2027–JAN 2028: Link to chemical evolution. Contrast Z_* vs $12 + \log(\text{O}/\text{H})$ residuals; understand the differences; environment trends.
- FEB–MAR 2028: Paper. Consolidate results, finalize figures/tables, archive products, submit Paper 3.

4 Project Management

4.1 Milestones

- Commencement: 07/04/2025
- M1 (Month 6): 09/2025, 6-month PhD proposal review.
- M2 (Month 12): 03/2026, PhD first year review.
- M3 (Month 24): 03/2027, PhD second year review.
- M4 (Month 36): 03/2028, PhD third year review.

4.2 Data Management

MAUVE-MUSE and MAUVE-ALMA data are stored in Data Central, CANFAR and my laptop.

4.3 Supervision and Meeting Plan

Principal & Coordinating supervisor: Prof. Luca Cortese 80%.

Co-supervisor: A/Prof. Luke Davies 20%.

Meeting: I have a weekly meeting with Prof. Luca Cortese, A/Prof Luke Davies and Prof. Barbara Catinella to provide updates and discuss my project. I also attend the weekly group meeting led by Prof. Luca Cortese and Prof. Barbara Catinella.

4.4 Training & Confirmation Tasks

- ACRI9000 Academic Integrity: completed on 10/04/2025.
- PHYS5003 Scientific Communication for Physicists: completed on 01/07/2025.

Bibliography

- Andrade A., Saviane I., Monaco L., Yegorova I., Proust D., 2024, [A&A](#), **686**, A81
- Bacon R., et al., 2017, [A&A](#), **608**, A1
- Baker W. M., Maiolino R., Bluck A. F. L., Lin L., Ellison S. L., Belfiore F., Pan H.-A., Thorp M., 2022, [MNRAS](#), **510**, 3622
- Baker W. M., et al., 2023, [MNRAS](#), **519**, 1149
- Barrera-Ballesteros J. K., et al., 2016, [MNRAS](#), **463**, 2513
- Belfiore F., Vincenzo F., Maiolino R., Matteucci F., 2019, [MNRAS](#), **487**, 456
- Boselli A., Gavazzi G., 2006, [PASP](#), **118**, 517
- Boselli A., et al., 2014, [A&A](#), **570**, A69
- Boselli A., et al., 2018, [A&A](#), **614**, A56
- Boselli A., et al., 2023, [A&A](#), **669**, A73
- Bothwell M. S., Maiolino R., Kennicutt R., Cresci G., Mannucci F., Marconi A., Cicone C., 2013, [MNRAS](#), **433**, 1425
- Bothwell M. S., Maiolino R., Peng Y., Cicone C., Griffith H., Wagg J., 2016, [MNRAS](#), **455**, 1156
- Bouché N. F., 2017, in Fox A., Davé R., eds, *Astrophysics and Space Science Library Vol. 430, Gas Accretion onto Galaxies*. p. 355 ([arXiv:1612.00740](#)), [doi:10.1007/978-3-319-52512-9_15](#)
- Bouché N., et al., 2010, [ApJ](#), **718**, 1001
- Bulichi T.-E., et al., 2023, [A&A](#), **679**, A98
- Bundy K., et al., 2015, [ApJ](#), **798**, 7
- Calzetti D., Armus L., Bohlin R. C., Kinney A. L., Koornneef J., Storchi-Bergmann T., 2000, [ApJ](#), **533**, 682
- Calzetti D., et al., 2007, [ApJ](#), **666**, 870
- Cano-Díaz M., et al., 2016, [ApJL](#), **821**, L26
- Cappellari M., 2023, [MNRAS](#), **526**, 3273

- Chabrier G., 2003, [PASP](#), **115**, 763
- Cortese L., Catinella B., Smith R., 2021, [PASA](#), **38**, e035
- Cresci G., Mannucci F., Curti M., 2019, [A&A](#), **627**, A42
- Croom S. M., et al., 2012, [MNRAS](#), **421**, 872
- Curti M., Mannucci F., Cresci G., Maiolino R., 2020, [MNRAS](#), **491**, 944
- Davé R., Finlator K., Oppenheimer B. D., 2012, [MNRAS](#), **421**, 98
- Davies L. J. M., et al., 2019, [MNRAS](#), **483**, 5444
- Davies L. J. M., Fuentealba-Fuentes M. F., Wright R. J., Bravo M., Wagh S., Siudek M., 2025, [MNRAS](#), **541**, 3220
- Dayal P., Ferrara A., Dunlop J. S., 2013, [MNRAS](#), **430**, 2891
- Dopita M. A., Kewley L. J., Sutherland R. S., Nicholls D. C., 2016, [Ap&SS](#), **361**, 61
- Ellison S. L., Simard L., Cowan N. B., Baldry I. K., Patton D. R., McConnachie A. W., 2009, [MNRAS](#), **396**, 1257
- Emsellem E., et al., 2022, [A&A](#), **659**, A191
- Foster C., et al., 2021, [PASA](#), **38**, e031
- Franchetto A., et al., 2021, [ApJ](#), **923**, 28
- Fraser-McKelvie A., et al., 2024, [arXiv e-prints](#), p. arXiv:2411.03430
- Gao Y., et al., 2018, [ApJ](#), **869**, 15
- Garcia A. M., et al., 2024, [MNRAS](#), **531**, 1398
- Genzel R., et al., 2010, [MNRAS](#), **407**, 2091
- Hsieh B. C., et al., 2017, [ApJL](#), **851**, L24
- Jaffé Y. L., et al., 2018, [MNRAS](#), **476**, 4753
- Kashibadze O. G., Karachentsev I. D., Karachentseva V. E., 2020, [A&A](#), **635**, A135
- Kauffmann G., et al., 2003, [MNRAS](#), **346**, 1055
- Kewley L. J., Dopita M. A., Sutherland R. S., Heisler C. A., Trevena J., 2001, [ApJ](#), **556**, 121
- Kewley L. J., Groves B., Kauffmann G., Heckman T., 2006, [MNRAS](#), **372**, 961
- Kewley L. J., Nicholls D. C., Sutherland R. S., 2019, [ARA&A](#), **57**, 511
- Koller M., et al., 2024, [A&A](#), **689**, A315
- Krumholz M. R., Dekel A., 2012, [ApJ](#), **753**, 16

- Lara-López M. A., et al., 2010, [A&A](#), **521**, L53
- Lara-López M. A., et al., 2022, [A&A](#), **660**, A105
- Leslie S. K., et al., 2020, [ApJ](#), **899**, 58
- Lian J., Thomas D., Li C., Zheng Z., Maraston C., Bizyaev D., Lane R. R., Yan R., 2019, [MNRAS](#), **489**, 1436
- Lilly S. J., Carollo C. M., Pipino A., Renzini A., Peng Y., 2013, [ApJ](#), **772**, 119
- Looser T. J., D'Eugenio F., Piotrowska J. M., Belfiore F., Maiolino R., Cappellari M., Baker W. M., Tacchella S., 2024, [MNRAS](#), **532**, 2832
- Maier C., et al., 2016, [A&A](#), **590**, A108
- Mannucci F., Cresci G., Maiolino R., Marconi A., Gnerucci A., 2010, [MNRAS](#), **408**, 2115
- Mei S., et al., 2007, [ApJ](#), **655**, 144
- Obreja A., Brook C. B., Stinson G., Domínguez-Tenreiro R., Gibson B. K., Silva L., Granato G. L., 2014, [MNRAS](#), **442**, 1794
- Pallottini A., Ferrara A., Gallerani S., Sommovigo L., Carniani S., Vallini L., Kohandel M., Venturi G., 2025, [A&A](#), **699**, A6
- Peng Y.-j., Maiolino R., 2014, [MNRAS](#), **438**, 262
- Peng Y., Maiolino R., Cochrane R., 2015, [Nature](#), **521**, 192
- Pessa I., et al., 2021, [A&A](#), **650**, A134
- Pietrinferni A., Cassisi S., Salaris M., Hidalgo S., 2013, [A&A](#), **558**, A46
- Pilyugin L. S., Grebel E. K., 2016, [MNRAS](#), **457**, 3678
- Pilyugin L. S., Tautvaišienė G., 2024, [A&A](#), **682**, A41
- Poggianti B. M., et al., 2017, [ApJ](#), **844**, 48
- Rybizki J., Just A., Rix H.-W., 2017, [A&A](#), **605**, A59
- Sánchez S. F., et al., 2012, [A&A](#), **538**, A8
- Sánchez S. F., et al., 2013, [A&A](#), **554**, A58
- Sánchez S. F., et al., 2017, [MNRAS](#), **469**, 2121
- Sánchez S. F., et al., 2019, [MNRAS](#), **484**, 3042
- Sanders R. L., et al., 2021, [ApJ](#), **914**, 19
- Schaefer A. L., et al., 2019, [ApJ](#), **884**, 156

- Speagle J. S., Steinhardt C. L., Capak P. L., Silverman J. D., 2014, [ApJS](#), **214**, 15
- Thorne J. E., et al., 2021, [MNRAS](#), **505**, 540
- Tremonti C. A., et al., 2004, [ApJ](#), **613**, 898
- Vazdekis A., et al., 2015, [MNRAS](#), **449**, 1177
- Wang E., Lilly S. J., 2023, [ApJ](#), **955**, 55
- Watts A. B., et al., 2024, [MNRAS](#), **530**, 1968
- Weilbacher P. M., et al., 2020, [A&A](#), **641**, A28
- Whitaker K. E., et al., 2014, [ApJ](#), **795**, 104
- Yao Y., Chen G., Liu H., Chen X., Lin Z., Zhang H.-X., Gao Y., Kong X., 2022, [A&A](#), **661**, A112
- Yates R. M., Kauffmann G., 2014, [MNRAS](#), **439**, 3817
- Yates R. M., Kauffmann G., Guo Q., 2012, [MNRAS](#), **422**, 215
- Zabel N., et al., 2024, [MNRAS](#), **535**, 2538

A Timeline Visualization

